

A Decentralized Higher Order Sliding Mode Control for Islanded Photovoltaic- Storage Systems

A. Rosini¹, R. Procopio¹, A. Bonfiglio¹, G. P. Incremona² and A. Ferrara³

¹ University of Genoa – Department of Electrical, Electronic, Telecommunications
Engineering and Naval Architecture.

Via Opera Pia 11a – I-16145

Genoa - Italy

² Dipartimento di Elettronica, Informazione e Bioingegneria, Politecnico di Milano,
20133 Milan, Italy.

³ Dipartimento di Ingegneria Industriale e dell'Informazione, University of Pavia,
27100 Pavia, Italy.

Corresponding author: Prof. Andrea Bonfiglio
University of Genoa – Department of Electrical, Electronic,
Telecommunications Engineering and Naval Architecture.
Via Opera Pia 11a – I-16145
Genoa - Italy
a.bonfiglio@unige.it

Abstract

Sustainable energy transition, air pollution reduction and climate change mitigation are the most challenging themes in nowadays energy sector. Microgrids (MGs) are one of the most effective ways to integrate Renewable Energy Sources (RES), and among them PhotoVoltaic (PV)-Storage (ST) configuration is relevantly promising. Focusing the attention on the PV and ST converters primary control, the main needs are to properly regulate voltage and frequency and optimally exploit the energy coming from the sun and manage the ST operation without any communication among the converter controllers. The conventional converter control approach presents several drawbacks and thus a strategy based on Higher Order Sliding Mode (HOSM) is presented in this work. The HOSM converter control strategy is fully analysed defining its control laws and the control schemes. A comparison between the HOSM and conventional control is performed with dedicated simulations on a common benchmark MG in order to highlight the advantages of the proposed strategy.

Keywords: Islanded Microgrids, Grid Feeding Inverters, Grid Forming inverters, Sliding Mode Control.

1. INTRODUCTION

One of the most important challenges of the energy sector for the current century is the massive deployment of Renewable Energy Sources (RES) to aim at sustainable energy transition, air pollution reduction, and consequently climate change mitigation [1]. In this energy scenario, a very effective way to flexibly and efficiently integrate RES sources into the energy mix is represented by Microgrids (MGs). MGs will play a central role in the new energy paradigm. A MG is defined as an integrated energy system consisting of Distributed Energy Resources (DERs) and multiple electrical loads operating as a single grid either in parallel to or islanded from the existing distribution grid [2]. Among all MGs typologies, one of the most promising is the so-called islanded Photovoltaic (PV)-Storage (ST) configuration [3]. This type of MG is an interesting solution due to its flexibility and sustainability [4].

Nevertheless, considering the unpredictable behaviour of the solar power and the necessity of proper managing the ST State Of Charge (SOC), the PV and the ST inverters controllers have to be thoroughly designed to guarantee the continuity of supply of the MG load and meet the standard quality requirements (e.g. IEEE St.1547 [5]).

Several types of controllers have been proposed to properly manage MG converters, such as Proportional-Integral (PI) controllers [6, 7], resonant controllers [8], \mathcal{H}_∞ controllers [9] or Model Predictive Control (MPC) based controllers [10, 11]. Also FBL and L_2 gain have been used recently in [12] and [13] respectively in wind turbine converters.

In this frame, the literature about control of islanded PV-ST configurations was deeply investigated. In particular, [14] proposed a PV-ST management where each generation unit is equipped with a dedicated local primary controller based on PI regulators. The main drawback is that the control structure is complicated with multiple feedback loops and pulse-width modulation, which leads to slow dynamic response. Secondly, the tuning of PI parameters is time-consuming and lacks of generality (as totally empirical), and this makes the controller implementation more complicated.

For this reason, the adoption of some advanced control methods to islanded PV-ST MGs has been recently investigated: among them it is worth citing the MPC and the Sliding Mode (SM) controllers.

In particular in [11, 15, 16], the MPC approach has been adopted for the primary control of islanded MGs. It must be underlined that [11, 15, 16] are one of the very few cases where MPC is proposed for the converter control rather than for the secondary or tertiary ones. However, MPC has several drawbacks if applied to the primary control level and the most relevant is the difficulty/impossibility to provide fast control action for the converter modulation due to the high CPU effort required to solve numerically an optimization problem at each simulation step.

SM controllers have also been applied to MG converter control [17-19]. This is a promising approach due to its robustness properties against a wide class of uncertainties [20]. Moreover, SM control belongs to the class of variable structure control systems, which looks perfectly adequate for the control of power electronic converters. In fact, power electronic systems represent a typical example in which discontinuous control is intrinsically provided [21].

An important application of SM controllers can be found in [22] where a perturbation observer based fractional-order SM has been proposed in the grid-connected configuration. Despite the excellent results obtained, the dynamic behaviour of an islanded MG with a Grid Forming converter has not been analyzed. Authors of [23] propose a novel SM controller for supercapacitor energy storage system, but also in this case only the grid connected configuration is analysed and the transition between different operating modes is not taken into account.

Two different operation modes are defined: the Normal Operation (NO) in which the PV unit works at its Maximum Power Point (MPP) and so it is in Grid-Feeding mode [24] and the ST maintains the instantaneous power balance, (i.e. Grid-Forming mode), and the Power (SOC) Priority (PP or SP), where the ST exchanged power is fixed and the PV is curtailed to act as a Slack bus.

The main innovative contributions of the proposed decentralized SM based architecture are:

- combining the advantages of the droop and master/slave controllers [25] (no communication needed and frequency and voltage restoration);
- defining suitable converter controllers capable to manage the ST SoC and power limitations and PV converters curtailment;
- guaranteeing an automatic and seamless transition among the different MG operating assets without any communication among the controllers.
- combining in one (local) controller for each device the control goals of traditional primary and secondary frequency regulation. This latter usually requires a centralized controller and thus a communication network among the DERs controllers.

The paper is organized as follows: Section II provides a summary of the control objectives and features of the proposed approach, Section III describes the SM controllers during the NO scenario, while Section IV proposes a modification in the SM controllers to properly manage the PV power curtailment (PP mode). Section V reports a detailed set of simulations to show the proper operation of the proposed approach and its advantages over conventional controllers based on PI regulators. Final remarks are reported in Section VI.

2. STATEMENT OF THE PROBLEM AND CONTROL SYSTEM STRUCTURE

The work aims at developing a Higher Order Sliding Mode (HOSM) based control system that allows islanded MG composed of PV units and Storage system to:

- regulate frequency and voltage;
- satisfy the load demand;
- consider the physical characteristics of both DERs.

These points are to be satisfied without communication infrastructure between PV and ST units. As explained in the previous section, two different operating modes are

considered: the NO and the PP (or SP) which starts when the ST reaches its maximum absorbable active power limit ($P_{ST,lim}$) or SoC limit (SoC_{lim}). When this happens, a logic signal $PP_{on}(SP_{on})$ is used internally by the ST HOSM controller to switch the control from the Grid-Forming mode to the Grid-Feeding mode. As the power absorbed by the battery is fixed, the PV has to reduce its power production to maintain the power balance and so to switch its operating mode from Grid-Feeding mode to Grid-Forming mode. To have a communication-less approach this change in the PV unit operating mode has to be applied without any communication infrastructure. It has been demonstrated in [26] that the measured frequency at the output of the PV converter $f_{PV,meas}$ starts to increase when the ST converter switches from NO to PP (or SP) mode and the PV converter is still in NO operating mode. For this reason, when $f_{PV,meas}$ reaches a threshold value f_{PP} , an internal signal $PV_{forming}$, activates the Grid-Forming operating mode of the PV converter and the PV system switches from NO to PP mode (without any communication infrastructure).

The control logic is sketched in the flowchart of Fig. 1.

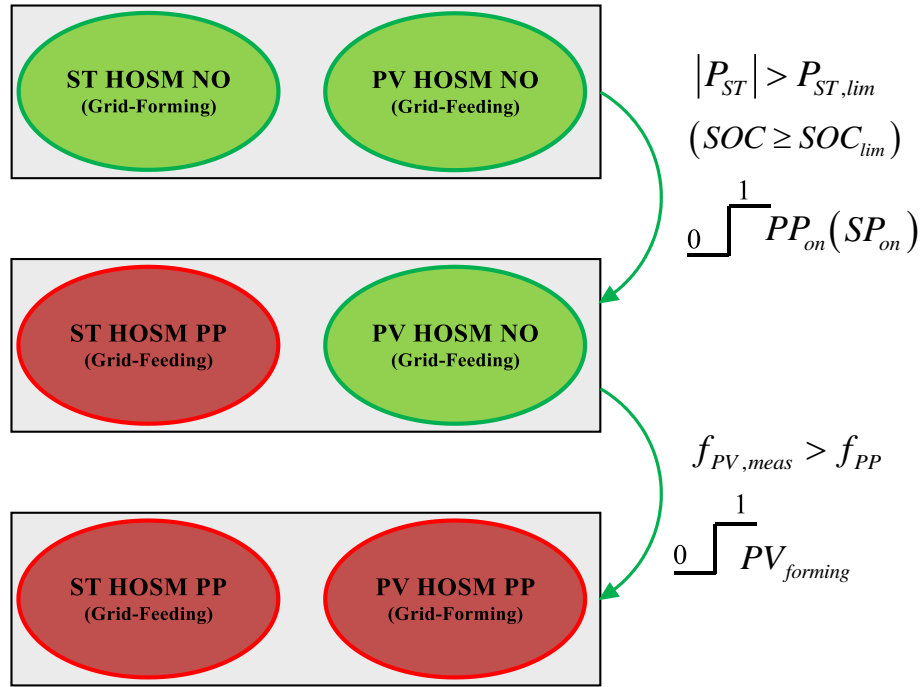


Fig. 1: Flowchart of the transition logic between operating modes.

As specified before, all the controllers sketched in Fig. 1 are HOSM based for the following reasons. From a computational effort perspective, HOSM controllers present the same cost as classic PI controllers, as they do not need to implement any numerical method (unlike MPC that requires the numerical solution of an optimization problem at each step). Moreover, compared with classic PI approach, HOSM controllers show the following advantages:

- robustness properties against a wide class of uncertainties, in particular of matched type [20];
- the system stability can be analytically demonstrated;
- as will be clarified later on, the control matrices are diagonal (or triangular) and so it is possible to decouple the control channels with two scalar regulators and no feedforward actions are required (that, being model dependent, do not guarantee an effective decoupling when working on real systems);
- the tuning procedure of the controller gains is easier because precise rules based on stability conditions have been provided in [27]. Moreover, in contrast to classic approaches, there is no need of implementing nested loops (e.g. voltage loop and current inner loop [28]) whose parameters setting relies on empirical procedure and stability is not guaranteed;

In the following sub-sections, the HOSM controllers for the MG operating modes are fully described for both PV and ST converter units.

3. NORMAL OPERATION

During NO the PV unit produces active power following the power reference coming from its MPPT algorithm and reactive power satisfying the Energy Management System (EMS) request. The ST unit, instead, controls voltage and frequency at the output of the harmonic filter of its converter. The detailed controller design for the two units in NO is hereafter provided.

3.1 ST System

The ST system model considered for the controller design is depicted in Fig. 2, where $E(SOC)$ is the internal voltage that depends on the SOC of the ST, R_{int} , L_{int} and C_{DC} are the internal resistance, internal inductance and the DC link capacitor respectively. The harmonic filter is modelled as a resistance R_f , an inductance L_f and a shunt capacitance C_f . Then, V_{DC} is the DC link voltage, while I_S is the DC ST current. The converter line to ground three-phase output voltages are $e_{abc}^{(i)}$ while the converter output currents are $i_{abc}^{(i)}$. The voltages at the shunt filter capacitor are $e_{abc}^{(g)}$ and finally the currents injected into the grid are $i_{abc}^{(g)}$.

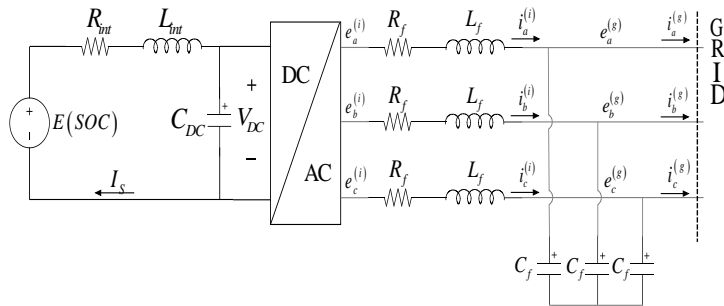


Fig. 2: ST System electric model.

Kirchhoff Current and Voltage Laws applied to the AC portion of circuit of Fig. 2 and written in a Park reference frame synchronous with the inverter angular frequency reference $\omega_p = \dot{\theta}_p$ (which is an assigned value, e.g. 314 rad/s in Europe) allow to write:

$$\left\{ \begin{array}{l} \dot{i}_d^{(i)} = -\frac{R_f}{L_f} i_d^{(i)} + \omega_p i_q^{(i)} - \frac{e_d^{(c)}}{L_f} + \frac{V_{DC} u_d^{(i)}}{L_f} \\ \dot{i}_q^{(i)} = -\frac{R_f}{L_f} i_q^{(i)} - \omega_p i_d^{(i)} - \frac{e_q^{(c)}}{L_f} + \frac{V_{DC} u_q^{(i)}}{L_f} \\ \dot{e}_d^{(c)} = \frac{i_d^{(i)}}{C_f} + \omega_p e_q^{(c)} - \frac{i_d^{(g)}}{C_f} \\ \dot{e}_q^{(c)} = \frac{i_q^{(i)}}{C_f} - \omega_p e_d^{(c)} - \frac{i_q^{(g)}}{C_f} \end{array} \right. \quad (1)$$

where subscripts d and q refer to direct and quadrature axis components of voltages and currents.

The inputs of the ST system are the dq components of the modulation signals, which are related to the dq components of the converter output voltages as follows:

$$\begin{bmatrix} u_d^{(i)} \\ u_q^{(i)} \end{bmatrix} = \frac{1}{V_{DC}} \begin{bmatrix} e_d^{(i)} \\ e_q^{(i)} \end{bmatrix} \quad (2)$$

Moreover, assuming to measure the DC voltage V_{DC} , one can avoid involving the DC side equations in the design of the ST inverter controller (note that a dedicated battery controller that regulates V_{DC} always exists).

The system state vector is therefore defined as:

$$\underline{x} = \begin{bmatrix} i_d^{(i)} & i_q^{(i)} & e_d^{(c)} & e_q^{(c)} \end{bmatrix}^T \quad (3)$$

while ST voltage control is obtained if the output vector is:

$$\underline{y} = \begin{bmatrix} e_d^{(c)} \\ e_q^{(c)} \end{bmatrix} \quad (4)$$

Now it is possible to perform the derivative of the output vector to obtain the relative degree of the system. It is easy to see that:

178

$$\begin{cases} \ddot{e}_d^{(c)} = f_{ST,d}(\underline{x}) + \frac{V_{DC} \dot{u}_d^{(i)}}{L_f C_f} \\ \ddot{e}_q^{(c)} = f_{ST,q}(\underline{x}) + \frac{V_{DC} \dot{u}_q^{(i)}}{L_f C_f} \end{cases} \quad (5)$$

179

where $f_{ST,d}(\underline{x})$ and $f_{ST,q}(\underline{x})$ collect all quantities that do not contain the input. So the control matrix $G_{ST}(\underline{x})$ is given by:

180

181

$$G_{ST}(\underline{x}) = \frac{V_{DC}}{L_f C_f} \begin{bmatrix} 1 & 0 \\ 0 & 1 \end{bmatrix} \quad (6)$$

182

Given these considerations, since we have in mind to design a HOSM control aimed at chattering alleviation [29], an auxiliary system with relative degree equal to 1 is needed. Indeed, if the relative degree of the auxiliary system is equal to 1, the HOSM control can be designed so as to artificially increase that relative degree from 1 to 2, thus transforming the classical sliding mode control problem into a sliding mode control problem of the second order, as illustrated in [27]. This latter can be solved by designing a discontinuous control acting on the second time derivative of the sliding variable. This implies that the designed discontinuous control input, i.e., the control input appearing in the auxiliary system after the relative degree increment, is passed through an integrator to generate the actual control input to be fed into the plant. As a consequence, the actual plant control input results in being a continuous signal, which significantly mitigates the possible chattering effect. Hence, it is possible to choose the sliding variables as follows:

183

184

185

$$\sigma_{d,NO} = \lambda_{1d} (\dot{e}_d^{(c)} - \dot{e}_d^{(c)*}) + \lambda_{2d} (e_d^{(c)} - e_d^{(c)*}) \quad (7)$$

186

$$\sigma_{q,NO} = \lambda_{1q} (\dot{e}_q^{(c)} - \dot{e}_q^{(c)*}) + \lambda_{2q} (e_q^{(c)} - e_q^{(c)*}) \quad (8)$$

187

$e_{d(q)}^{(c)*}$ being the capacitor voltage direct (quadrature) axis reference. It is apparent that the relative degree in this case is 1, so that by computing the second derivative of (7) and (8) it is possible to obtain:

188

189

$$\ddot{\sigma}_{d,NO} = F_{ST,d}(\underline{x}, u_d^{(i)}) + \lambda_{1d} \left(\frac{V_{DC} \ddot{u}_d^{(i)}}{L_f C_f} \right) \quad (9)$$

190

$$\ddot{\sigma}_{q,NO} = F_{ST,q}(\underline{x}, u_q^{(i)}) + \lambda_{1q} \left(\frac{V_{DC} \ddot{u}_q^{(i)}}{L_f C_f} \right) \quad (10)$$

where $F_{ST,d}(\underline{x}, u_d^{(i)})$ and $F_{ST,q}(\underline{x}, u_q^{(i)})$ collect all the variables that do not depend on the input derivatives, and the new input variable is given by the derivative of the actual control input. In other words, an integrator, receiving in input the discontinuous control, is added, so that the control signal actually fed into the plant is a continuous signal, with beneficial effects in term of chattering alleviation. Rewriting (9) and (10) in matrix form, one has:

$$\begin{bmatrix} \ddot{\mathbf{o}}_{d,NO} \\ \ddot{\mathbf{o}}_{q,NO} \end{bmatrix} = \begin{bmatrix} F_{ST,d}(\underline{x}, \mathbf{u}_d^{(i)}) \\ F_{ST,q}(\underline{x}, \mathbf{u}_q^{(i)}) \end{bmatrix} + [G_{ST}(\underline{x})] \begin{bmatrix} \dot{\mathbf{u}}_d^{(i)} \\ \dot{\mathbf{u}}_q^{(i)} \end{bmatrix} \quad (11)$$

Since the elements of $F_{ST,d}(\underline{x}, u_d^{(i)})$, $F_{ST,q}(\underline{x}, u_q^{(i)})$ and $G_{ST}(\underline{x})$ have bounded uncertainties (a limited upper-bounded exists), the diagonality of matrix $G_{ST}(\underline{x})$ allows to conclude that the two scalar control laws [27]:

$$\dot{u}_d^{(i)} = -U_d \text{sign}(\sigma_{d,NO} - 0.5 \sigma_{d,NO,max}) \quad (12)$$

$$\dot{u}_q^{(i)} = -U_q \text{sign}(\sigma_{q,NO} - 0.5 \sigma_{q,NO,max}) \quad (13)$$

(U_d and U_q being suitable gains) guarantee the system stability [19]. The ST converter control system in NO is reported in Fig. 3. Note that (5) is a multivariable system with relative degree equal to 4. Thus the system does not exhibit any internal dynamics.

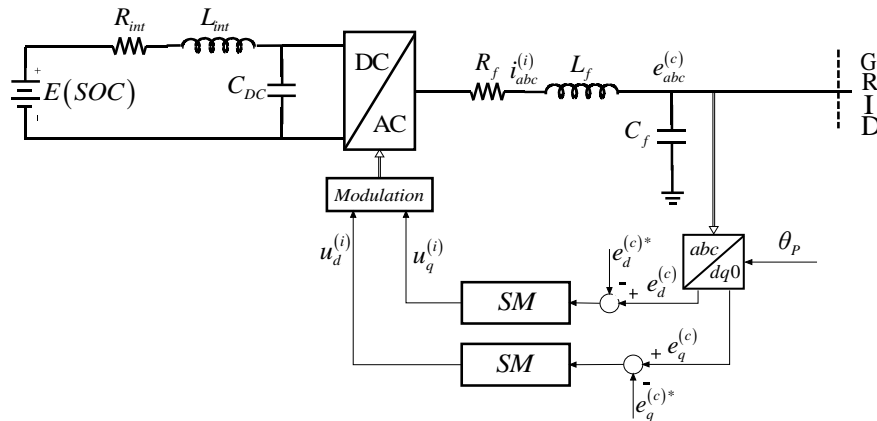


Fig. 3: ST converter control system for NO.

3.2 PV System

The electric model of the PV system is depicted in Fig. 4 where the DC link voltage is V_{DC} , the DC PV current is I_{PV} , while the PV panel voltage is V_{PV} . With a slight abuse of notation, the nomenclature of the AC side is the same as the one used for the ST system.

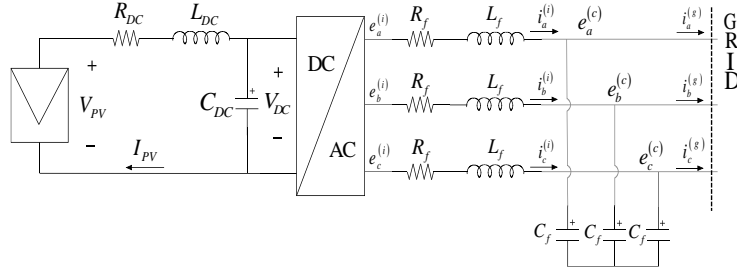


Fig. 4: PV System electric model.

Considering again a Park reference frame synchronous with the inverter angular frequency $\omega_p = \dot{\theta}_p$, the dynamic equations of the PV system are:

$$\begin{cases} V_{DC} I_{PV} - V_{DC} C_{DC} \dot{V}_{DC} = e_d^{(i)} i_d^{(i)} + e_q^{(i)} i_q^{(i)} \\ V_{PV}(I_{PV}, \alpha, T) - R_{DC} I_{PV} - L_{DC} \dot{I}_{PV} = V_{DC} \end{cases} \quad (14)$$

where $V_{PV}(I_{PV}, \alpha, T)$ is the functional relationship between PV voltage, and current, solar irradiance and panel temperature [30] and:

$$\begin{cases} \dot{i}_d^{(i)} = -\frac{R_f}{L_f} i_d^{(i)} + \omega_p i_q^{(i)} - \frac{e_d^{(c)}}{L_f} + \frac{e_d^{(i)}}{L_f} \\ \dot{i}_q^{(i)} = -\frac{R_f}{L_f} i_q^{(i)} - \omega_p i_d^{(i)} - \frac{e_q^{(c)}}{L_f} + \frac{e_q^{(i)}}{L_f} \\ \dot{e}_d^{(c)} = \frac{i_d^{(i)}}{C_f} + \omega_p e_q^{(c)} - \frac{i_d^{(g)}}{C_f} \\ \dot{e}_q^{(c)} = \frac{i_q^{(i)}}{C_f} - \omega_p e_d^{(c)} - \frac{i_q^{(g)}}{C_f} \end{cases} \quad (15)$$

In this case, the state vector is:

$$\underline{x} = [I_{PV} \ V_{DC} \ i_d^{(i)} \ i_q^{(i)} \ e_d^{(c)} \ e_q^{(c)}]^T \quad (16)$$

The inputs are the dq components of the modulating signals, i.e.:

$$\underline{u} = \begin{bmatrix} u_d^{(i)} \\ u_q^{(i)} \end{bmatrix} = \frac{1}{V_{DC}} \begin{bmatrix} e_d^{(i)} \\ e_q^{(i)} \end{bmatrix}. \quad (17)$$

As far as the output vector is concerned, one component is the PV panel voltage is V_{PV} that has to track its MPP V_{PV}^* . Reactive power control Q_{PV} can be performed aligning the Park transform with the voltage at the capacitor bus in order to obtain that:

$$Q_{PV} = -e_d^{(c)} i_q^{(g)} \quad (18)$$

So, measuring the capacitor voltage amplitude, the reactive power can be regulated controlling the q -axis current injected at the point of connection with the grid. Moreover, measuring the capacitor quadrature axis current $i_q^{(c)}$ and observing that:

$$i_q^{(i)} = i_q^{(c)} + i_q^{(g)} \quad (19)$$

one can choose as output vector the following:

$$\underline{F} \underline{y} = \begin{bmatrix} V_{PV} \\ i_q^{(i)} \end{bmatrix} \quad (20)$$

Neglecting the dependence of the PV panel voltage V_{PV} on the irradiance and temperature (they have a slow variation in the primary regulation time frame), one obtains that:

$$\ddot{V}_{PV}(I_{PV}, \alpha, T) = f_{PV,V}(\underline{x}) + \frac{\partial V_{PV}(I_{PV})}{\partial I_{PV}} \frac{1}{L_{DC} C_{DC}} (u_d^{(i)} i_d^{(i)} + u_q^{(i)} i_q^{(i)}) \quad (21)$$

where $f_{PV,V}(\underline{x})$ collects all the quantities that do not depend on the input. Moreover:

$$\dot{i}_q^{(i)} = -\frac{R_f}{L_f} i_q^{(i)} - \omega_p i_d^{(i)} - \frac{e_q^{(c)}}{L_f} + \frac{e_q^{(i)}}{L_f} = f_{PV,Q}(x) + \frac{V_{DC} u_q^{(i)}}{L_f} \quad (22)$$

So the dynamic of the system is given by:

$$\begin{cases} \ddot{V}_{PV} = f_{PV,V}(x) + \frac{\partial V_{PV}(I_{PV})}{\partial I_{PV}} \frac{1}{L_{DC} C_{DC}} (u_d^{(i)} i_d^{(i)} + u_q^{(i)} i_q^{(i)}) \\ \dot{i}_q^{(i)} = f_{PV,Q}(x) + \frac{V_{DC} u_q^{(i)}}{L_f} \end{cases} \quad (23)$$

and the control matrix is:

$$G_{PV}(x) = \begin{bmatrix} \frac{\partial V_{PV}(I_{PV})}{\partial I_{PV}} \frac{i_d^{(i)}}{L_{DC} C_{DC}} & \frac{\partial V_{PV}(I_{PV})}{\partial I_{PV}} \frac{i_q^{(i)}}{L_{DC} C_{DC}} \\ 0 & \frac{V_{DC}}{L_f} \end{bmatrix} \quad (24)$$

Defining the two sliding variables in order to have relative degree 1 as follows

$$\sigma_{d,NO} = \lambda_{1d} (\dot{V}_{PV} - \dot{V}_{PV}^*) + \lambda_{2d} (V_{PV} - V_{PV}^*) \quad (25)$$

257 and

$$258 \quad \sigma_{q,NO} = i_q^{(i)} - i_{q,ref}^{(i)} \quad (26)$$

259 one has that:

$$260 \quad \ddot{\sigma}_{d,NO} = F_{PV,V}(\underline{x}, u_d^{(i)}, u_q^{(i)}) + \lambda_{1d} \left[\frac{\partial V_{PV}(I_{PV})}{\partial I_{PV}} \frac{i_d^{(i)}}{L_{DC} C_{DC}} \right] \dot{u}_d^{(i)} + \quad (27)$$

$$+ \lambda_{1d} \left[\frac{\partial V_{PV}(I_{PV})}{\partial I_{PV}} \frac{i_q^{(i)}}{L_{DC} C_{DC}} \right] \dot{u}_q^{(i)}$$

$$261 \quad \ddot{\sigma}_{q,NO} = F_{PV,Q}(\underline{x}, u_q^{(i)}) + \frac{V_{DC} \dot{u}_q^{(i)}}{L_f} \quad (28)$$

262 where $F_{PV,V}(\underline{x}, u_d^{(i)})$ and $F_{PV,Q}(\underline{x}, u_q^{(i)})$ collect all the variables that do not depend on the
263 input derivatives. In matrix notation, it follows that:

$$264 \quad \begin{bmatrix} \ddot{\sigma}_{d,NO} \\ \ddot{\sigma}_{q,NO} \end{bmatrix} = \begin{bmatrix} F_{PV,V}(x) \\ F_{PV,Q}(x) \end{bmatrix} + \begin{bmatrix} G_{PV}(x) \end{bmatrix} \begin{bmatrix} \dot{u}_d^{(i)} \\ \dot{u}_q^{(i)} \end{bmatrix} \quad (29)$$

265 So the two scalar control laws allow to meet the control requirements:

$$266 \quad \dot{u}_d^{(i)} = -U_d \operatorname{sgn}(\sigma_{d,NO} - 0.5 \sigma_{d,NO,max}) \quad (30)$$

$$267 \quad \dot{u}_q^{(i)} = -U_q \operatorname{sgn}(\sigma_{q,NO} - 0.5 \sigma_{q,NO,max}) \quad (31)$$

268 To prove this fact, one has first to notice that if the variable $\sigma_{q,NO}$ becomes zero at a
269 finite time $\bar{t}_q \geq 0$, i.e.,

$$270 \quad \sigma_{q,NO} = i_q^{(i)} - i_{q,ref}^{(i)} = 0 \quad (32)$$

271 giving rise to a sliding mode on $\sigma_{q,NO} = 0$ when $\sigma_{d,NO} \neq 0$, then, by exploiting the
272 equivalent control concept, for any $t \geq \bar{t}_q$ it yields:

$$273 \quad \dot{\tilde{u}}_q(t) = - \frac{F_{PV,Q}(x(t)) L_f}{V_{DC}} \quad (33)$$

274 As a consequence, by integrating (33), one obtains:

$$275 \quad \tilde{u}_q(t) = \int_0^t - \frac{F_{PV,Q}(x(\tau)) L_f}{V_{DC}} d\tau \quad (34)$$

Since $F_{PV,Q}(x(t))$ is bounded due to the physical nature of the involved variables, then there exists:

$$\tilde{U}_q = \sup_{t \geq 0} |\tilde{u}_q(t)| \quad (35)$$

Hence, by virtue of (32) and (33), for any $t \geq \bar{t}_q$, the first equation in (23) can be replaced by:

$$\ddot{V}_{PV} = f_{PV,V}(x) + \frac{\partial V_{PV}(I_{PV})}{\partial I_{PV}} \frac{1}{L_{DC} C_{DC}} \left(u_d^{(i)} i_d^{(i)} + \tilde{u}_q^{(i)} i_{q,ref}^{(i)} \right) \quad (36)$$

which can be rewritten as:

$$\ddot{V}_{PV} = F_{PV,V} + \frac{\partial V_{PV}(I_{PV})}{\partial I_{PV}} \frac{1}{L_{DC} C_{DC}} u_d^{(i)} i_d^{(i)} \quad (37)$$

with:

$$F_{PV,V} = f_{PV,V}(x) + \frac{\partial V_{PV}(I_{PV})}{\partial I_{PV}} \frac{1}{L_{DC} C_{DC}} \tilde{u}_q^{(i)} i_{q,ref}^{(i)} \quad (38)$$

Relying on the knowledge of L_{DC} , C_{DC} , $i_{q,ref}^{(i)}$ and $\partial V_{PV}(I_{PV})/\partial I_{PV}$, of the upper-bound of $f_{PV,V}$, and of (35), a bound of $F_{PV,V}$ can be determined. According to Theorem 1 in [27], the control amplitude U_d in (30) can be chosen so that $\sigma_{d,NO}$ becomes zero in a finite time $\bar{t}_d > \bar{t}_q \geq 0$. In other terms, to design the sliding mode control components (30) and (31), one has to guarantee that the sliding variable $\sigma_{q,NO}$ is steered to zero when $\sigma_{d,NO}$ is still different from zero, enforcing the so-called hierarchy of control, in analogy with a similar approach proposed for first order sliding mode control systems in [31]. As previously discussed, when the hierarchy of control is enforced, the generation of second order sliding modes on $\sigma_{d,NO} = 0$ and $\sigma_{q,NO} = 0$ directly follows.

The PV converter control system in NO is reported in Fig. 5 where Q_{PV}^* is the reactive power reference.

where $H_{ST,d}(\underline{x})$ and $H_{ST,q}(\underline{x})$ are matrices that collect all the variables that do not depend on the input derivatives.

Here again the control matrix is diagonal, and the two scalar control laws are:

$$\begin{aligned}\dot{u}_d^{(i)} &= -U_d \operatorname{sgn}(\sigma_{d,PP} - 0.5 \sigma_{d,PP,max}) \\ \dot{u}_q^{(i)} &= -U_q \operatorname{sgn}(\sigma_{q,PP} - 0.5 \sigma_{q,PP,max})\end{aligned}\tag{43}$$

Regarding the stability of the internal dynamics, this analysis is reported in the Appendix B.

4.2 PV System

The dynamic equations that describe the PV system are still (14) and (15). The controlled variables are the dq voltage components at the output of the converter filter, so the control problem is the same as the ST system in NO.

5. SIMULATIONS RESULTS

This section aims at presenting the results of the simulations performed to compare the proposed HOSM control system in NO and PP with the conventional converter control based on PID regulators. More precisely, the ST unit has an outer PID voltage regulator and an inner PID current regulator in a cascade configuration, while the PV unit has only the PID current regulator and a PID DC voltage regulator (see [32] for details).

Unlike the model adopted for the controllers' design, the simulations have been performed in the Simulink/Simscape environment that allows a much more detailed representation of the MG chosen as a test case (depicted in Fig. 6). The significant difference between the two representation of the MG allows to test the robustness of the developed HOSM controllers against modelling and parametric uncertainties. In particular, the Simulink/Simscape model includes:

- detailed DC voltage sources for ST and PV units [33];
- MPPT based on both Perturb&Observe and Fractional Open Circuit method techniques [34];
- IGBT two-level inverters [21];
- LCL filters composed by the converter side resistance $R_{fc,PV(ST)}$ the converter side inductance $L_{fc,PV(ST)}$ the shunt capacitance $C_{f,PV(ST)}$, the grid side resistance $R_{fg,PV(ST)}$ and the grid side inductance $L_{fg,PV(ST)}$;
- connection resistance R_{line} and transformers;

- constant impedance three-phase load described by resistance R_{load} and inductance L_{load} .

All the relevant data are reported in

Table 1.

Table 1: MG main parameters.

Symbol	Description	Value	Symbol	Description	Value
V_n	Rated voltage (l-l, RMS)	400 V	$R_{fc,PV}$	PV Converter-side resistance	0.17 Ω
f_n	Rated frequency	50 Hz	$L_{fc,PV}$	PV Converter-side inductance	28 mH
f_{sw}	PWM converters switching frequency	10 kHz	$R_{fg,PV}$	PV Grid-side resistance	0.01 Ω
A_{ST}	ST converter rated power	6 kVA	$L_{fg,PV}$	PV Grid-side inductance	1.3 mH
A_{PV}	PV converter rated power	6 kVA	$C_{f,PV}$	PV Filter capacitor	4.7 μ F
$R_{fc,ST}$	ST Converter-side resistance	0.046 Ω	R_{line}	Cable resistance	0.02 Ω
$L_{fc,ST}$	ST Converter-side inductance	4 mH	R_{load}	Load resistance	18.5 Ω
$R_{fg,ST}$	ST Grid-side resistance	0.032 Ω	L_{load}	Load inductance	39 mH
$L_{fg,ST}$	ST Grid-side inductance	2.4 mH	$v\%,ST$	ST transformer short-circuit voltage	8%
$C_{f,ST}$	ST Filter capacitor	4.7 μ F	$v\%,PV$	PV transformer short-circuit voltage	8%

The controllers parameters are reported in Table 2. It is important to highlight that the tuning procedure with HOSM controllers is based on the try and error approach, but the theory provides the indication towards which to move the gains (increasing them) guaranteeing the system stability. The cascade structure of the PID does not allow to have criteria for moving the gains unless having a numerical code that calculates the eigenvalues as a function of the gains and numerically finding an n-uple that leads to negative eigenvalues.

So two important advantages of the HOSM controllers with respect to traditional PID ones can be highlighted:

- 1) HOSM theoretical results give a clear indication that control amplitudes have to be increased; on the other hand, when dealing with PID controls there are no available theoretical results that provides guidelines on how to adjust parameters of the controllers in order to meet stability conditions.

- 2) the traditional control system for these kinds of MGs is based on a nested structure of the controllers (primary controller, voltage loop and current loop) which increases the complexity of the system and the number of parameters to be selected.

Table 2: HOSM and PID parameters.

Symbol	Description	Value	Symbol	Description	Value
$U_{d,NO}^{ST}$	ST d -axis HOSM gain in NO	3500 V/s	f_{PP}	PV frequency threshold for PP	50.7 Hz
$U_{q,NO}^{ST}$	ST q -axis HOSM gain in NO	3500 V/s	$P_{ST,lim}$	ST maximum absorbable active power limit	700 W
$U_{d,PP}^{ST}$	ST d -axis HOSM gain in PP	3500 V/s	$K_{I,P}^{ST}$	ST current PID regulator proportional gain	15 V/A
$U_{q,PP}^{ST}$	ST q -axis HOSM gain in PP	3500 V/s	$K_{I,I}^{ST}$	ST current PID regulator integral gain	2000 V/As
$U_{d,NO}^{PV}$	PV d -axis HOSM gain in NO	3×10^4 V/s	$K_{V,P}^{ST}$	ST voltage PID regulator proportional gain	0.09 A/V
$U_{q,NO}^{PV}$	PV q -axis HOSM gain in NO	3×10^4 V/s	$K_{V,I}^{ST}$	ST voltage PID regulator integral gain	5 A/Vs
$U_{d,PP}^{PV}$	PV d -axis HOSM gain in PP	3×10^4 V/s	$K_{I,P}^{PV}$	PV current PID regulator proportional gain	35 V/A
$U_{q,PP}^{PV}$	PV q -axis HOSM gain in PP	3×10^4 V/s	$K_{I,I}^{PV}$	PV current PID regulator integral gain	200 V/As
			$K_{DC,P}^{PV}$	PV DC voltage PID regulator proportional gain	1 A/V
			$K_{DC,I}^{PV}$	PV DC voltage PID regulator integral gain	30 A/Vs

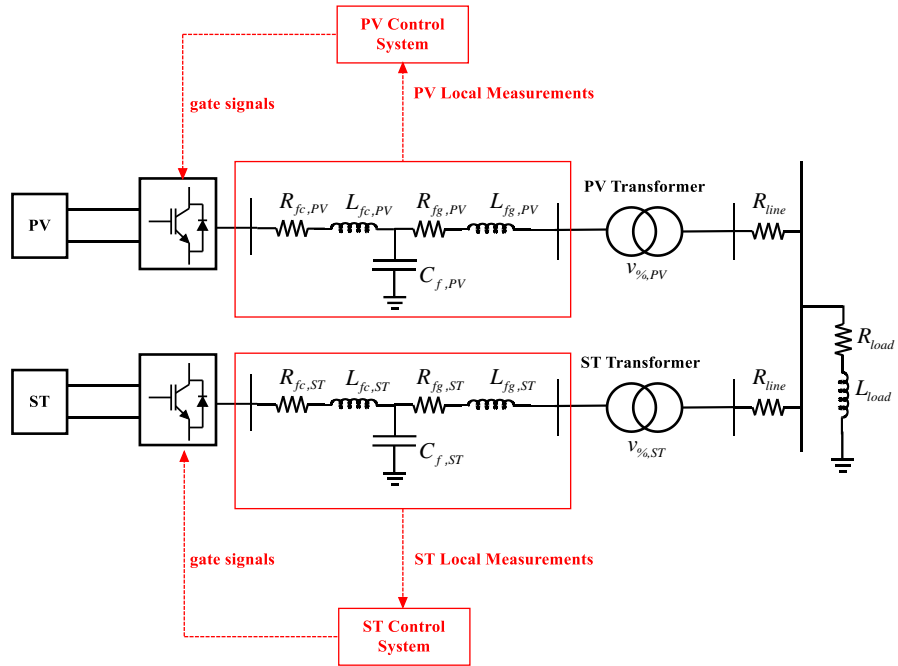


Fig. 6: MG model implemented in the Simscape environment.

A detailed control scheme for the implementation of HOSM controllers is depicted in Fig. 7

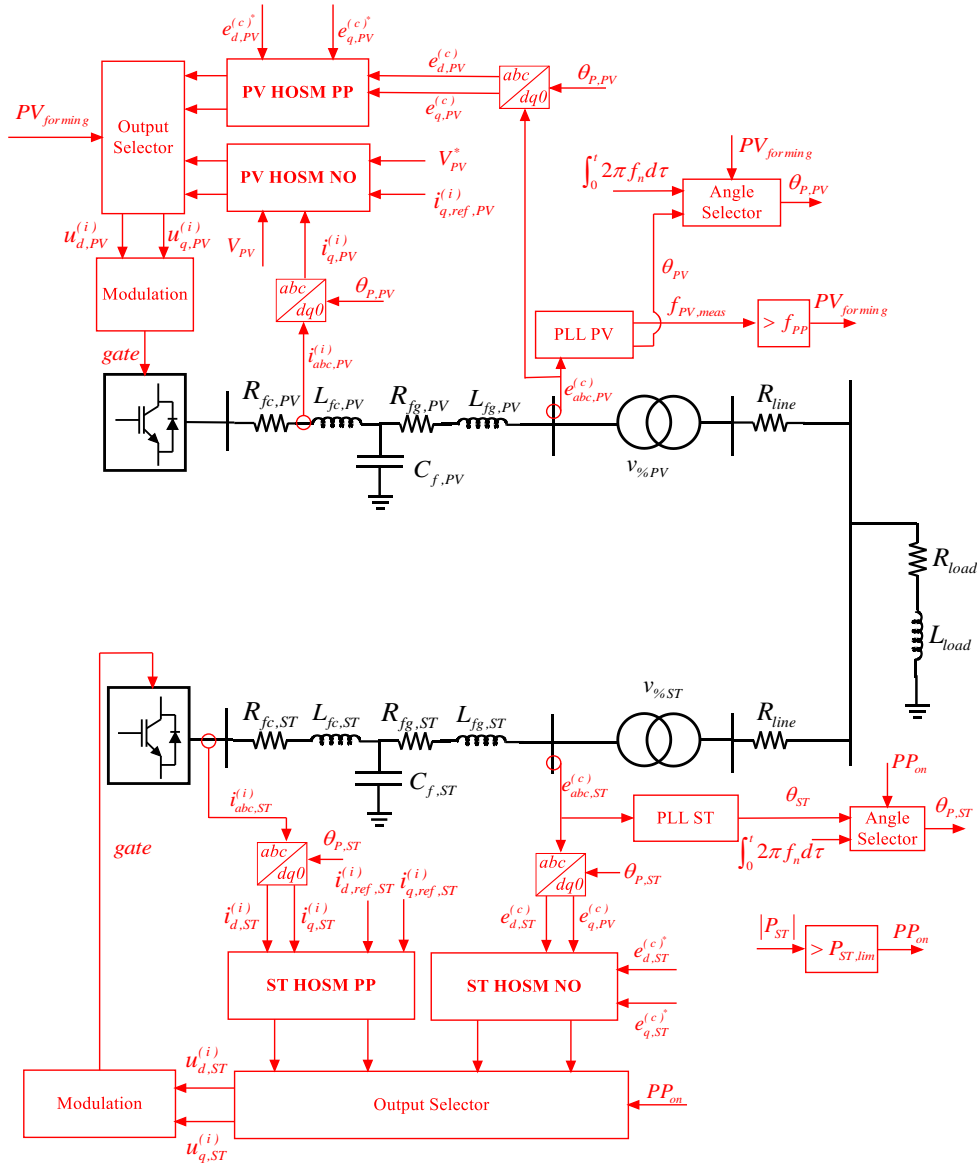


Fig. 7: Overall HOSM controllers implementation scheme.

5.1 Simulation A: irradiance variation in NO

In this first simulation, a twice irradiance variation is implemented. At $t = 3$ s the irradiance α varies from 500 W/m^2 to 800 W/m^2 . Then at $t = 5$ s the irradiance returns to the initial value of 500 W/m^2 . In Fig. 8 the DC voltage-time profile of the PV unit is reported. As one can see, the HOSM control can better track the voltage reference coming from the MPPT if compared to the PI control approach. No overshoot can be appreciated in the HOSM approach and a shorter settling time is guaranteed.

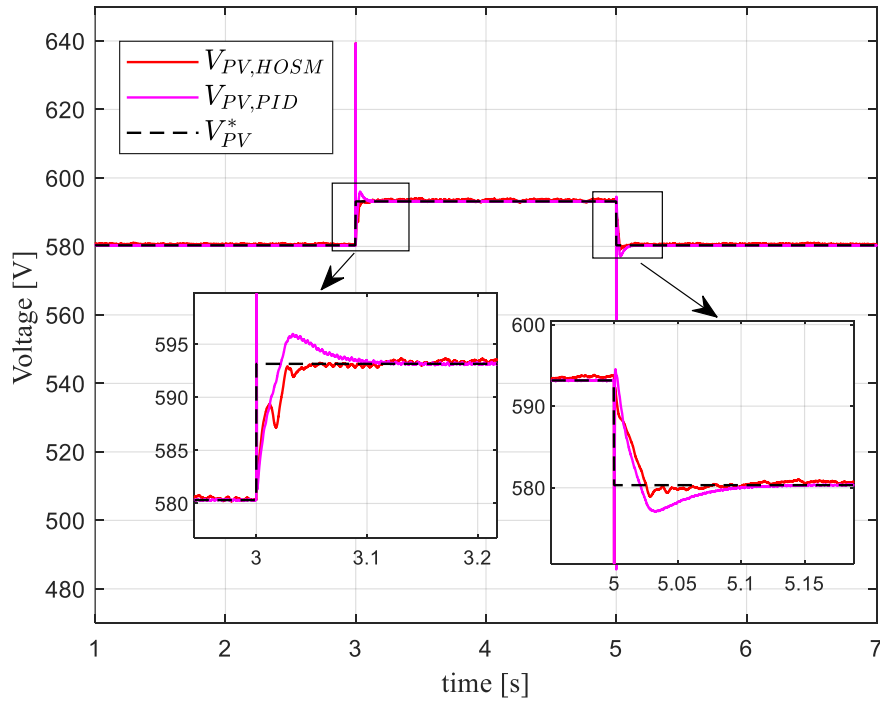


Fig. 8: PV voltage time profile during irradiance variation. Comparison with PID.

The same thing can be appreciated also in the active power time profiles reported in Fig. 9.

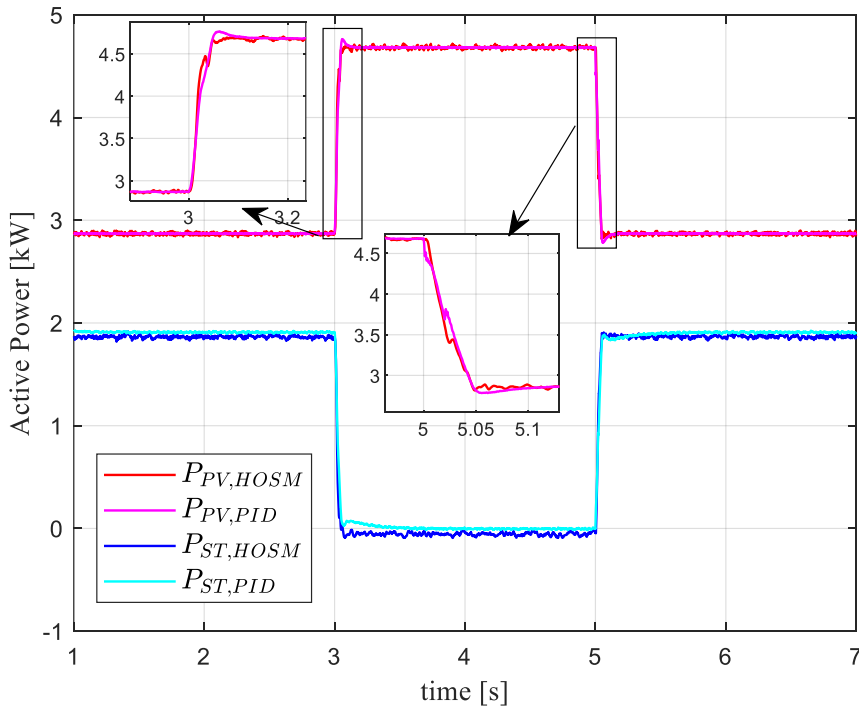


Fig. 9: Active powers time profile during irradiance variation. Comparison with PID.

Finally, the reactive powers time profile is reported in Fig. 10 and it is easy to see that, during the irradiance step variation, the PV HOSM control guarantees a significantly

better decoupling between the channels, as the reactive power provided by the PV presents a much smoother and faster dynamics than the PID case.

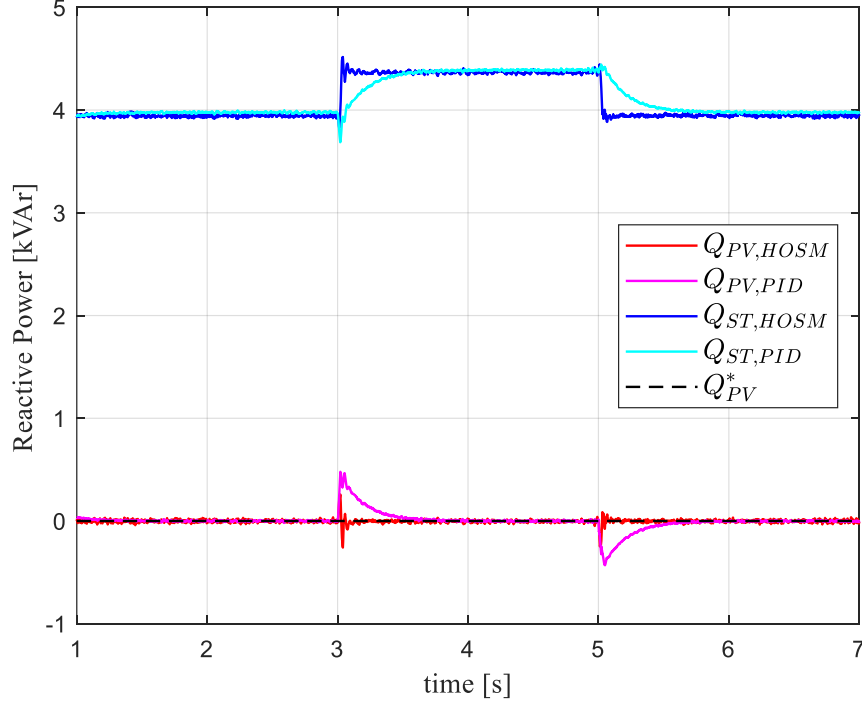


Fig. 10: Reactive powers time profile during irradiance variation. Comparison with PID.

Moreover, this first simulation allows to highlight the robustness of the proposed controllers against parameters uncertainties. In Fig. 11, the differences between the converter actual output voltages and the corresponding control inputs are reported. These differences are due to parameter uncertainties given by the modulation of the converter IGBTs which introduces harmonics in the system. The fact that second order sliding modes are generated by applying the proposed controllers, in spite of such differences, shows that it is capable of completing compensating for them, which demonstrates the controllers robustness.

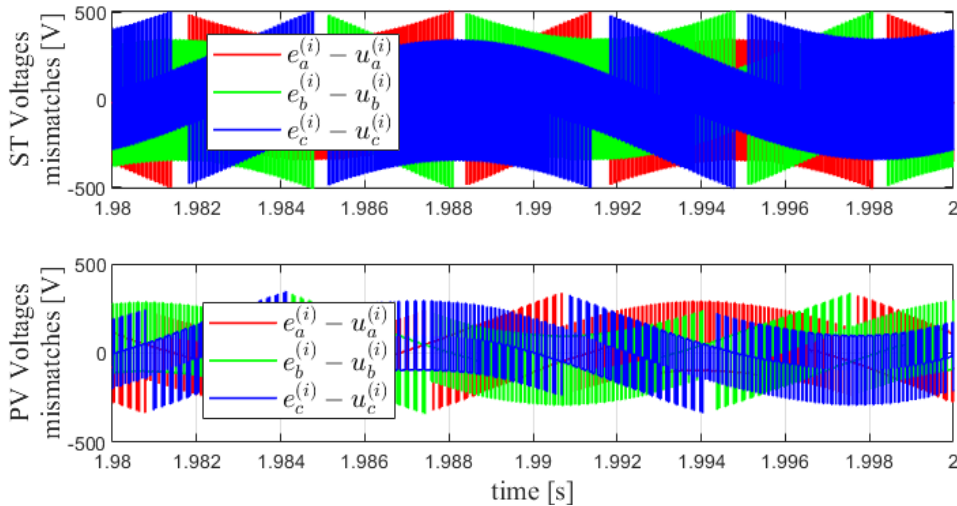


Fig. 11: Difference between the converter actual output voltages and the corresponding control inputs.

5.2 Simulation B: Reactive power reference variation in NO

In this second simulation, the system response to a reactive power reference step is reported. At $t = 2$ s the PV system reactive power reference Q_{PV}^* varies from 0 kVAr to 1 kVAr. Then at $t = 4$ s Q_{PV}^* is moved to -1 kVAr. Finally, at $t = 6$ s it returns to 0 kVAr. As one can see from Fig. 12, the PV HOSM can better track the DC reference voltage during reactive power reference steps compared to the PI approach which presents some overshoot. The reactive powers time profile is reported in Fig. 13 where it can be seen that the HOSM controller determines a smoother dynamics than the PI one; in particular the settling time of HOSM is about 50 ms, while PI needs more than 200 ms.

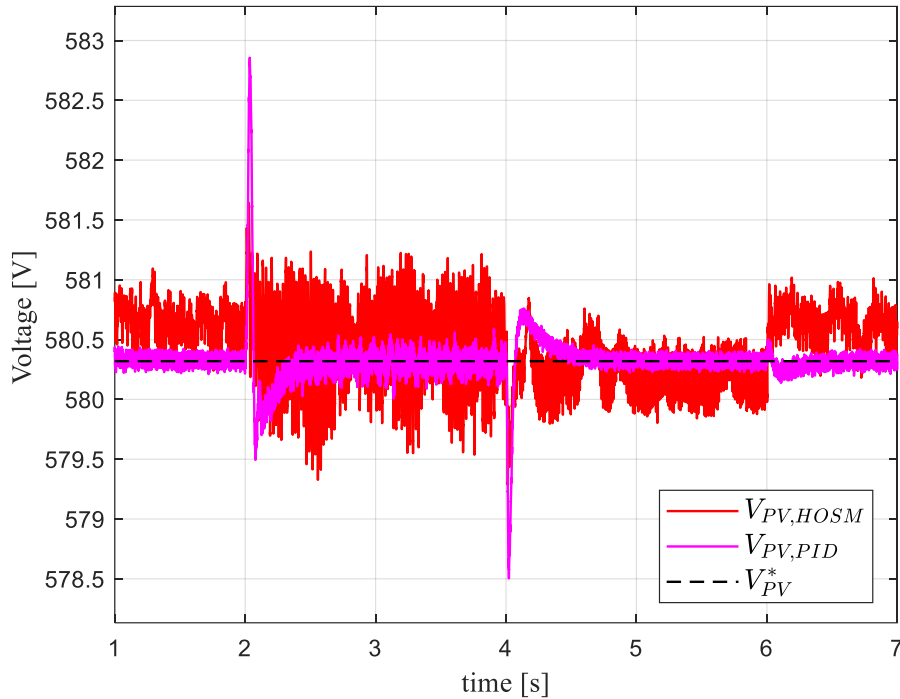


Fig. 12: PV voltage time profile during a reactive power reference variation. Comparison with PID.

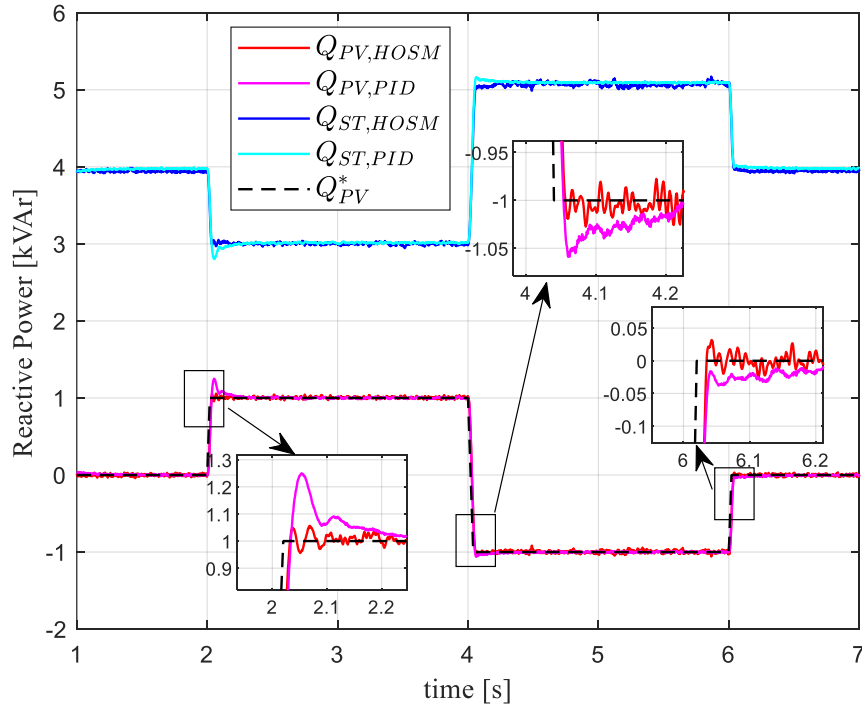


Fig. 13: Reactive powers time profile during a reactive power reference variation. Comparison with PID.

5.3 Simulation C: transition between NO and PP

In this last simulation, the results of the transition from NO to PP mode are reported. The ST unit controls its AC terminal voltage with a PID controller and implements a droop characteristic for its frequency control (droop coefficient equal to 1%). The PV unit works as an active and reactive power source thanks to its current control loop, but also accounting for the possibility of curtailing its active power reference in accordance to the system frequency variation (Limited Frequency Sensitive Mode-Over-frequency [35]). The PV Power curtailment characteristic is depicted in Fig. 14.

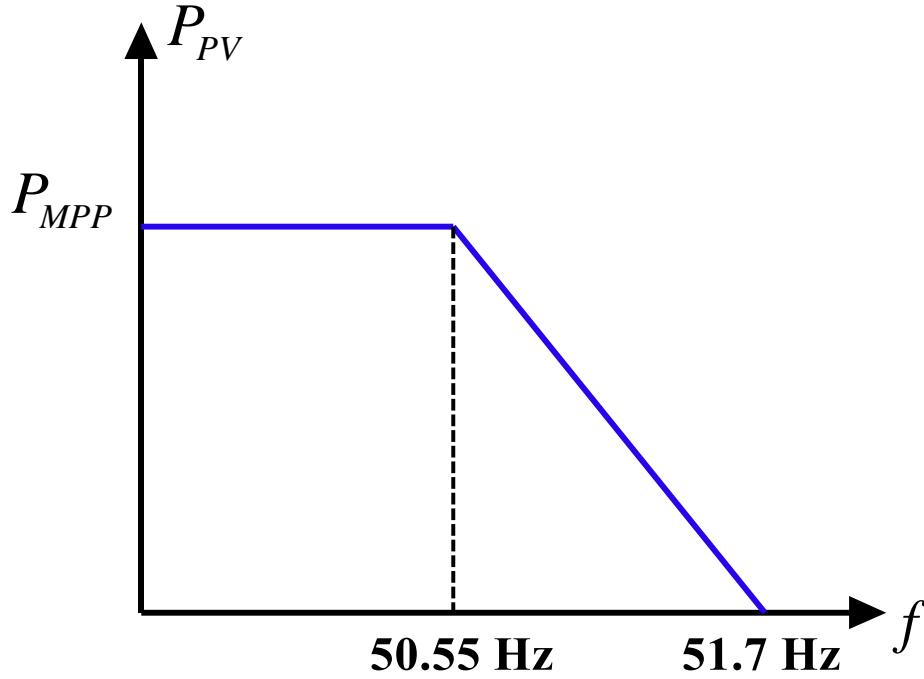


Fig. 14: PV unit power curtailment characteristic for the PID control .

At $t = 3$ s, the irradiance α exhibits a ramp variation from 500 W/m^2 to 1000 W/m^2 . As one can see from Fig. 15, at $t = 3.24$ s, the ST unit reaches $P_{ST,lim}$ and so it switches from NO to PP mode. Then, between $t = 3.24$ s and $t = 3.29$ s, both PV and ST units are in Grid Feeding configuration. In this frame, the measured frequency $f_{PV,meas}$ at the output of the PV converter increases; when it reaches the threshold value f_{pp} equal to 50.7 Hz, the PV converter enters in PP mode and it starts to control frequency and voltage acting as a Grid-Forming converter. It is possible to see that after a transient of about 600 ms the frequency returns to the reference value f_{ref} . On the other hand, with the PID control approach, the measured frequency at the output of the PV converter reaches the value of 50.7 Hz due to the droop coefficient in the ST converter control and it remains at this value (there is a steady-state error) because, with the conventional approach, there are not transitions between Grid-Forming and Grid-Feeding operations. Then, the dynamic of the PV DC voltage is reported in Fig. 16. When the PV enters in PP mode the MPPT value is not tracked because in this operating mode the PV unit has to control voltage and frequency and not to maximize the active power production. Moreover, it is possible to see that the PV DC voltage at steady state with HOSM is less than the one given by PID controllers and this means that with the HOSM controllers the PV unit is less curtailed compared to the conventional approach and this aspect is confirmed by the active power profiles depicted in Fig. 17.

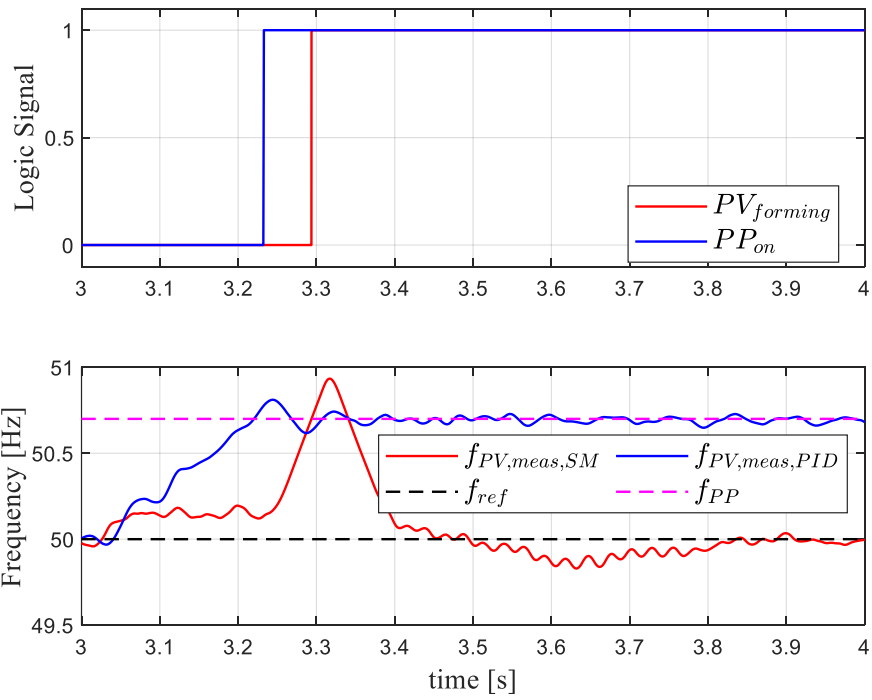


Fig. 15: Activation of the transition between operational modes.

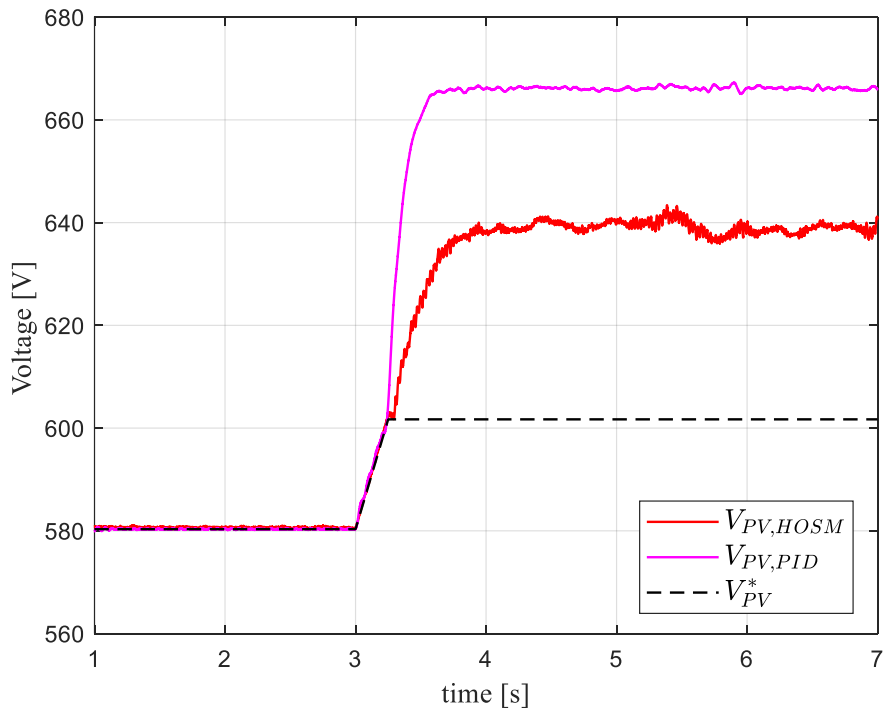


Fig. 16: PV voltage time profile during the transition between NO and PP Comparison with PID.

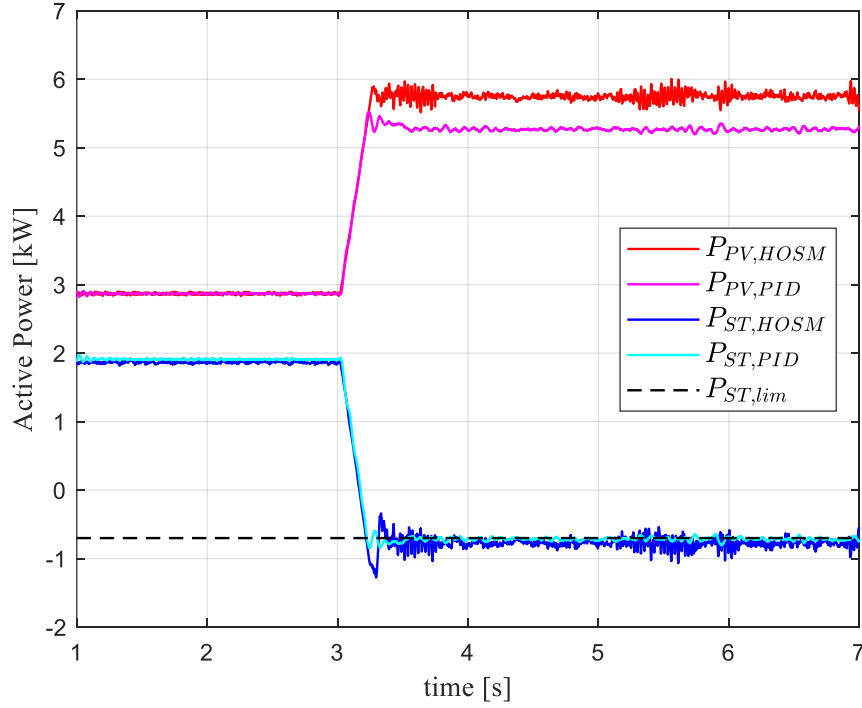


Fig. 17: Active powers time profile during the transition between NO and PP Comparison with PID.

5.4 Comparison with MPC

Focusing the attention on paper [11], the same authors of the present work proposed a decentralized approach for frequency and voltage regulation for PV-Storage MG based on MPC technique. However, from a general point of view, MPC presents some drawbacks that are listed below:

- high computational effort: if the implicit MPC is implemented, at each regulation step, an optimization problem must be solved numerically which claims for a very performing CPU and a moderately small set of constraints;
- robustness against parametric uncertainties is not guaranteed; so, if the system auxiliary model that is part of the optimization problem is not sufficiently close to reality, the control action may be ineffective;
- when different operation modes have to be guaranteed by the MPC controllers, the variables to be controlled are normally changed by modifying the weights in the objective function. The tuning of such weights is really critical because it is normally a matter of a try and error procedure.

On the other hand, HOSM controllers do not need the implementation of any numerical method and have been designed to cope with parametric uncertainties. For this reason, they seem to be promising for overcoming the aforementioned MPC drawbacks. A synoptic comparison between HOSM and MPC can be found in Table 3.

Table 3: Comparison between HOSM and MPC.

	HOSM	MPC
Robustness	High	Low

Control response	Fast	Slow
Computational effort	Low	High
Tuning procedure effort	Low	High
Hardware implementation effort	Low	High

Moreover in [11] some specific weak points can be highlighted:

- The AC inverter terminal voltage control is implemented using a steady-state approximate relation (i.e. the industrial voltage drop formula) and forcing such voltage to belong to an acceptable range; consequently a suitable reference value tracking is not guaranteed;
- According to the developed model, the reactive power produced by converters, being neither a state nor an input, cannot be directly controlled. A relation with states and inputs must be then derived and linearized to encode its control in the classic MPC formulation, thus introducing a certain degree of approximation against which the controller robustness is questionable.

Following this lead, the present article has pursued the same objective as [11], that is to say designing local inverter controllers that fully exploit the features of the HOSM control (i.e. chattering alleviation, robustness, and fast control actions) providing a plug-and-play architecture for the islanded PV-ST system. The proposed algorithm meets both the primary and secondary control goals (sharing the load request among the sources and zeroing the frequency errors) without the need for an ICT infrastructure that provides measurements communication among the converter controllers (i.e. the proposed control system is based only on local measurements).

The use of HOSM instead of MPC is justified by the above analysis; moreover, it is apparent that the two specific drawbacks of [11] are overcome because it is possible to directly control inverter AC terminal voltage and reactive power flow.

6. CONCLUSION

This paper proposed a control strategy based on HOSM control for ST and PV converters connected in parallel in an islanded AC MG considering different operating scenarios. The ST HOSM control has been designed to control voltage and frequency in NO, while the PV one to properly follow the active power reference coming from an MPPT algorithm and directly control the reactive power production. Then, the operating scenario in which the ST unit reaches its operating power limit absorption has been fully investigated and a communication-less transition in the controllers actions has been proposed to properly control the system in this condition too. Finally, a validation of the proposed approach has been proposed comparing its performances with the conventional control approach based on PID regulators. Simulations showed the effectiveness of the proposed strategy in terms of control response speed; moreover, the transition between the operating modes proved a better frequency regulation and a more successful exploitation of the PV energy. Future studies will include: *i*) the analysis of the proposed controllers also in the grid-connected configuration with the focus on transition between different operating modes, *ii*) the hardware implementation of the proposed controllers in order to validate their correct functioning through Hardware In

the Loop (HIL) simulations and experimental tests, *iii*) extension of the proposed controller to more sophisticated MGs (like the ones with conventional energy sources like CHP units or Diesel generators) and *iv*) extension of the proposed control approach to manage problems of faults in MGs.

7. APPENDIX: INTERNAL DYNAMICS STABILITY PROOF

7.1 PV internal dynamics stability in NO

As the relative degree of the PV dynamic system is 3, it is necessary to check the stability of the inner dynamic. Following the procedure reported in [36], and indicating with $[z_1, z_2, z_3]^T = [V_{PV}, \dot{V}_{PV}, i_q^{(i)}]^T$ the state of the internal dynamics after the application of a diffeomorphism $\Psi(x)$, it is necessary to define three new states Ψ_1, Ψ_2, Ψ_3 so that the transformation:

$$\begin{bmatrix} z_1 \\ z_2 \\ z_3 \\ \Psi_1 \\ \Psi_2 \\ \Psi_3 \end{bmatrix} = \Psi \left(\begin{bmatrix} x_1 \\ x_2 \\ x_3 \\ x_4 \\ x_5 \\ x_6 \end{bmatrix} \right) \quad (A1)$$

Ψ_1, Ψ_2, Ψ_3 can be chosen to satisfy:

$$\begin{cases} \frac{-i_d^{(i)}}{C_{DC}} \frac{\partial \Psi_i}{\partial x_1} + \frac{V_{DC}}{L_f} \frac{\partial \Psi_i}{\partial x_3} = 0 \\ \frac{-i_d^{(i)}}{C_{DC}} \frac{\partial \Psi_i}{\partial x_1} + \frac{V_{DC}}{L_f} \frac{\partial \Psi_i}{\partial x_4} = 0 \end{cases} \quad (A1)$$

$i = 1, 2, 3$

which are satisfied for example by:

$$\begin{cases} \Psi_1 = C_{DC} \frac{V_{DC}^2}{2} + \frac{L_f}{2} (i_d^{(i)2} + i_q^{(i)2}) \\ \Psi_2 = e_d^{(c)} \\ \Psi_3 = e_q^{(c)} \end{cases} \quad (A)$$

Indicating with:

$$I_{PV} = \zeta_{PV,a,T}(V_{PV}) \quad (47)$$

the (decreasing) function linking the PV unit voltage and current, and with:

$$\zeta_{PV,a,T} = \zeta_{PV,a,T}^{-1} \quad (48)$$

its inverse, the transformation thus defined is a diffeomorphism as the Jacobian matrix has a determinant given by:

$$\det J = L_f i_d^{(i)} \left[\frac{d\zeta_{PV,a,T}}{dI_{PV}} \right]^2 \quad (49)$$

which is non-zero if the PV unit produces active power.

So the internal dynamic is given by:

$$\begin{cases} \dot{\psi}_1 = V_{DC} I_{PV} - R_f \left(i_d^{(i)2} + i_q^{(i)2} \right) - e_q^{(c)} i_q^{(i)} - e_d^{(c)} i_d^{(i)} \\ \dot{\psi}_2 = \dot{e}_d^{(c)} = \frac{i_d^{(i)}}{C_f} + \omega_p e_q^{(c)} - \frac{i_d^{(g)}}{C_f} \\ \dot{\psi}_3 = \dot{e}_q^{(c)} = \frac{i_q^{(i)}}{C_f} - \omega_p e_d^{(c)} - \frac{i_q^{(g)}}{C_f} \end{cases} \quad (50)$$

The corresponding zero-dynamics is obtained by imposing:

$$\begin{bmatrix} z_1, z_2, z_3 \end{bmatrix}^T = \begin{bmatrix} V_{PV}, \dot{V}_{PV}, i_q^{(i)} \end{bmatrix}^T = \begin{bmatrix} V_{PV,MPP}, 0, i_{q,ref}^{(i)} \end{bmatrix}^T \quad (51)$$

The above position implies that the portion of the circuit upstream of the voltage on the DC side capacitor is at steady state, so one has:

$$V_{DC} \square V_{DC,ref} = V_{PV}^* - R_{DC} \zeta_{PV,a,T} \left(V_{PV,ref} \right) \quad (52)$$

So, inserting (51) and (52) in (A), it is possible to write:

$$\psi_1 = C_{DC} \frac{V_{DC,ref}^2}{2} + \frac{L_f}{2} \left(i_d^{(i)2} + i_{q,ref}^{(i)2} \right) \quad (53)$$

whose dynamics is:

$$\dot{\psi}_1 = L_f i_d^{(i)} i_d^{(i)} \quad (54)$$

Inserting (54) in (50) it is possible to write:

$$\left\{ \begin{array}{l} L_f \dot{i}_d^{(i)} i_d^{(i)} = V_{DC,ref} I_{PV,ref} - R_f \left(i_d^{(i)2} + i_{q,ref}^{(i)2} \right) - e_q^{(c)} i_{q,ref}^{(i)} - e_d^{(c)} i_d^{(i)} \\ \dot{e}_d^{(c)} = \frac{i_d^{(i)}}{C_f} + \omega_p e_q^{(c)} - \frac{i_d^{(g)}}{C_f} \\ \dot{e}_q^{(c)} = \frac{i_{q,ref}^{(i)}}{C_f} - \omega_p e_d^{(c)} - \frac{i_q^{(g)}}{C_f} \end{array} \right. \quad (55)$$

550 The analysis of the existence and stability of the equilibrium points of this system
 551 determines a possible restriction on the domain to which these inputs belong. The
 552 equilibrium point $(i_{d0}^{(i)}, e_{d0}^{(c)}, e_{q0}^{(c)})$ satisfies:

$$\left\{ \begin{array}{l} V_{DC,ref} I_{PV,ref} - R_f \left(i_{d0}^{(i)2} + i_{q,ref}^{(i)2} \right) - e_{q0}^{(c)} i_{q,ref}^{(i)} - e_{d0}^{(c)} i_{d0}^{(i)} = 0 \\ \frac{i_{d0}^{(i)}}{C_f} + \omega_p e_{q0}^{(c)} - \frac{i_d^{(g)}}{C_f} = 0 \\ \frac{i_{q,ref}^{(i)}}{C_f} - \omega_p e_{d0}^{(c)} - \frac{i_q^{(g)}}{C_f} = 0 \end{array} \right. \quad (56)$$

554 Solving system (56) it is possible to obtain:

$$555 \quad R_f i_{d0}^{(i)2} - \frac{1}{\omega_p C_f} i_q^{(g)} i_{d0}^{(i)} + R_f i_{q,ref}^{(i)2} - V_{DC,ref} I_{PV,ref} + \frac{i_d^{(g)} i_{q,ref}^{(i)}}{\omega_p C_f} = 0 \quad (57)$$

556 The discriminant of (57) is:

$$557 \quad \Delta = \left(\frac{1}{\omega_p C_f} i_q^{(g)} \right)^2 - 4 R_f \left(R_f i_{q,ref}^{(i)2} - V_{DC,ref} I_{PV,ref} + \frac{i_d^{(g)} i_{q,ref}^{(i)}}{\omega_p C_f} \right) \quad (58)$$

558 which is positive if:

$$559 \quad R_f i_{q,ref}^{(i)2} + \frac{i_d^{(g)}}{\omega_p C_f} i_{q,ref}^{(i)} - V_{DC,ref} I_{PV,ref} - \frac{1}{4 R_f} \left(\frac{1}{\omega_p C_f} i_q^{(g)} \right)^2 \leq 0 \quad (59)$$

560 So (59) gives a bounded set in which the q -axis reference current has to be contained.

561 So, solving (57), the d -axis current is given by:

$$562 \quad i_{d0}^{(i)} = \frac{\frac{1}{\omega_p C_f} i_q^{(g)} \pm \sqrt{\Delta}}{2 R_f} \quad (60)$$

563 while $e_{d0}^{(c)}$ and $e_{q0}^{(c)}$ can be found solving the second and the third of (55).

564 So, for a given independent input $i_q^{(g)}$, the equilibrium point exists if the control inputs
 565 V_{PV}^* , $i_{q,ref}^{(i)}$ satisfy (59); if this is the case, the equilibrium point can be found with (55)
 566 and (60).

567 Stability of such point can be assessed linearizing (55), which leads to the following
 568 state transition matrix:

$$569 \quad A = \begin{bmatrix} \frac{-2R_f i_{d0}^{(i)} - e_{d0}^{(c)}}{L_f i_{d0}^{(i)}} & -\frac{1}{L_f} & \frac{i_{q,ref}^{(i)}}{L_f i_{d0}^{(i)}} \\ \frac{1}{C_f} & 0 & \omega_p \\ 0 & -\omega_p & 0 \end{bmatrix} \quad (61)$$

570 whose eigenvalues are the solution of:

$$571 \quad \lambda^3 + \frac{2R_f i_{d0}^{(i)} + e_{d0}^{(c)}}{L_f i_{d0}^{(i)}} \lambda^2 + \left(\omega_p^2 + \frac{1}{L_f C_f} \right) \lambda + \omega_p^2 \frac{2R_f i_{d0}^{(i)} + e_{d0}^{(c)}}{L_f i_{d0}^{(i)}} + \frac{\omega_p i_{q,ref}^{(i)}}{C_f L_f i_{d0}^{(i)}} = 0 \quad (62)$$

572 Using the Routh–Hurwitz stability criterion, one gets the following conditions:

$$573 \quad \begin{aligned} & \omega_p^2 \frac{2R_f i_{d0}^{(i)} + e_{d0}^{(c)}}{L_f i_{d0}^{(i)}} + \frac{\omega_p i_{q,ref}^{(i)}}{C_f L_f i_{d0}^{(i)}} > 0 \\ & \frac{2R_f i_{d0}^{(i)} + e_{d0}^{(c)}}{L_f i_{d0}^{(i)}} > 0 \\ & \left(\omega_p^2 + \frac{1}{L_f C_f} \right) > \frac{\omega_p^2 \frac{2R_f i_{d0}^{(i)} + e_{d0}^{(c)}}{L_f i_{d0}^{(i)}} + \frac{\omega_p i_{q,ref}^{(i)}}{C_f L_f i_{d0}^{(i)}}}{\frac{2R_f i_{d0}^{(i)} + e_{d0}^{(c)}}{L_f i_{d0}^{(i)}}} \end{aligned} \quad (63)$$

574 Due to physical reasons, the second of (63) is always verified (PV injects active
 575 power and d component of the capacitor voltage equals its amplitude due to the choice
 576 of the Park transform), while the first one can be written as:

$$577 \quad \omega_p C_f e_{d0}^{(c)} + 2R_f \omega_p C_f i_{d0}^{(i)} + i_{q,ref}^{(i)} > 0 \quad (64)$$

and the third one as:

$$2R_f i_{d0}^{(i)} + e_{d0}^{(c)} > \omega_p L_f i_{q,ref}^{(i)} \quad (65)$$

Recalling (56) the zero-stability conditions are:

$$\begin{aligned} 2\omega_p R_f C_f i_{d0}^{(i)} + (1 - \omega_p^2 L_f C_f) i_{q,ref}^{(i)} - i_q^{(g)} &> 0 \\ 2i_{q,ref}^{(i)} - i_q^{(g)} + 2R_f \omega_p C_f i_{d0}^{(i)} &> 0 \end{aligned} \quad (66)$$

The above stability analysis has been performed on the MG described in Section V. As an example, supposing to set $i_q^{(g)}$ and

$V_{DC,ref} I_{PV,ref} = 6$ kW, the result of the zero-dynamics stability analysis appears in Fig. 18, where the light blue line represents the plot of (60), while the region that satisfies the two stability conditions is above the black and the red line. As can be deduced from the plot, all the existing equilibrium points are stable.

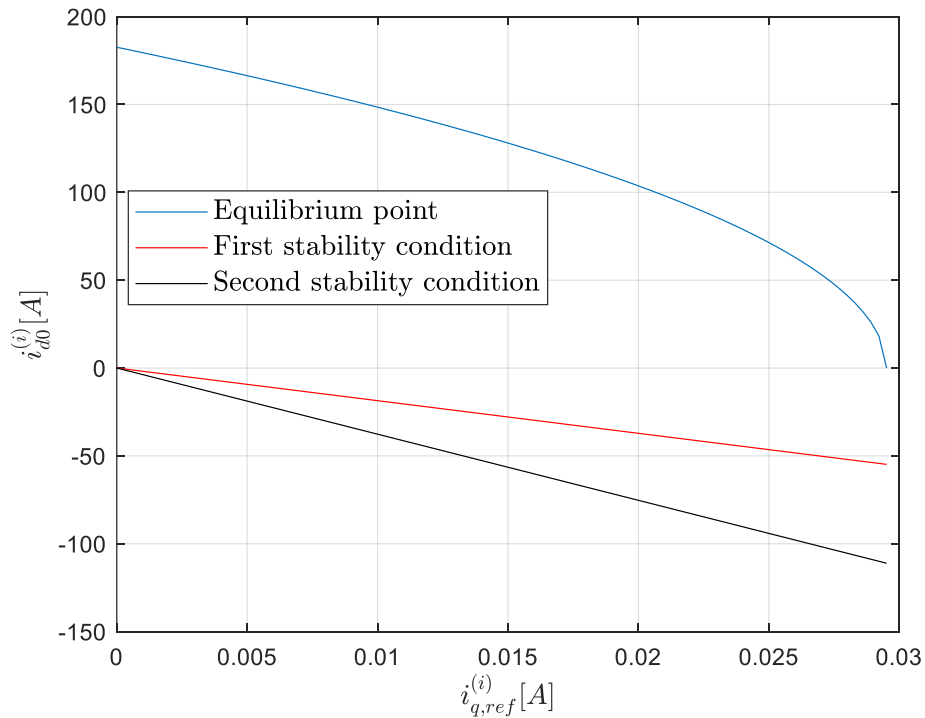


Fig. 18: Zero dynamics stability analysis for the PV unit in NO operating mode

7.2 ST internal dynamics stability in PP

With the same notations introduced in the previous subsection, it is possible to choose:

$$\begin{aligned} \psi_1 &= e_d^{(c)} \\ \psi_2 &= e_q^{(c)} \end{aligned} \quad (67)$$

So the state transformation is the identity matrix, and the internal dynamic is:

$$\begin{aligned}\dot{e}_d^{(c)} &= \frac{i_d^{(i)}}{C_f} + \omega_p e_q^{(c)} - \frac{i_d^{(g)}}{C_f} \\ \dot{e}_q^{(c)} &= \frac{i_q^{(i)}}{C_f} - \omega_p e_d^{(c)} - \frac{i_q^{(g)}}{C_f}\end{aligned}\tag{68}$$

Given the equilibrium point $\left(i_{d0}^{(i)} = i_{d,ref}^{(i)}, i_{q,ref}^{(i)}, e_{d0}^{(c)}, e_{q0}^{(c)}\right)$ and defined $\left(E_d^{(c)}, E_q^{(c)}\right) = \left(e_d^{(c)} - e_{d0}^{(c)}, e_q^{(c)} - e_{q0}^{(c)}\right)$, the zero-dynamic is given by:

$$\begin{aligned}\dot{E}_d^{(c)} &= \omega_p E_q^{(c)} \\ \dot{E}_q^{(c)} &= -\omega_p E_d^{(c)}\end{aligned}\tag{69}$$

which is linear with purely imaginary poles (thus limited, which is sufficient to guarantee the boundedness of all the states).

REFERENCES

- [1] F. Creutzig, P. Agoston, J. C. Goldschmidt, G. Luderer, G. Nemet, and R. C. Pietzcker, "The underestimated potential of solar energy to mitigate climate change," *Nature Energy*, vol. 2, no. 9, p. 17140, 2017/08/25 2017.
- [2] H. Jiayi, J. Chuanwen, and X. Rong, "A review on distributed energy resources and MicroGrid," *Renewable and Sustainable Energy Reviews*, vol. 12, no. 9, pp. 2472-2483, 2008/12/01/ 2008.
- [3] Y. Ghiassi-Farrokhfal, F. Kazhamiaka, C. Rosenberg, and S. Keshav, "Optimal Design of Solar PV Farms With Storage," *IEEE Transactions on Sustainable Energy*, vol. 6, no. 4, pp. 1586-1593, 2015.
- [4] W. Jing, C. H. Lai, W. S. H. Wong, and M. L. D. Wong, "A comprehensive study of battery-supercapacitor hybrid energy storage system for standalone PV power system in rural electrification," *Applied Energy*, vol. 224, pp. 340-356, 2018/08/15/ 2018.
- [5] "IEEE Standard for Interconnection and Interoperability of Distributed Energy Resources with Associated Electric Power Systems Interfaces," *IEEE Std 1547-2018 (Revision of IEEE Std 1547-2003)*, pp. 1-138, 2018.
- [6] H. Karimi, E. J. Davison, and R. Iravani, "Multivariable Servomechanism Controller for Autonomous Operation of a Distributed Generation Unit: Design and Performance Evaluation," *IEEE Transactions on Power Systems*, vol. 25, no. 2, pp. 853-865, 2010.
- [7] M. Babazadeh and H. Karimi, "A Robust Two-Degree-of-Freedom Control Strategy for an Islanded Microgrid," *IEEE Transactions on Power Delivery*, vol. 28, no. 3, pp. 1339-1347, 2013.
- [8] F. de Bosio, M. Pastorelli, L. d. S. Ribeiro, M. Lima, F. Freijedo, and J. M. Guerrero, "Current control loop design and analysis based on resonant regulators for microgrid applications," in *IECON 2015-41st Annual Conference of the IEEE Industrial Electronics Society*, 2015, pp. 005322-005327: IEEE.

- [9] T. Hornik and Q. Zhong, "A Current-Control Strategy for Voltage-Source Inverters in Microgrids Based on H_∞ and Repetitive Control," *IEEE Transactions on Power Electronics*, vol. 26, no. 3, pp. 943-952, 2011.
- [10] E. Mayhorn, K. Kalsi, J. Lian, and M. Elizondo, "Model predictive control-based optimal coordination of distributed energy resources," in *2013 46th Hawaii International Conference on System Sciences*, 2013, pp. 2237-2244: IEEE.
- [11] A. Rosini, D. Mestriner, A. Labella, A. Bonfiglio, and R. Procopio, "A decentralized approach for frequency and voltage regulation in islanded PV-Storage microgrids," *Electric Power Systems Research*, vol. 193, p. 106974, 2021/04/01/ 2021.
- [12] P. Li, L. Xiong, F. Wu, M. Ma, and J. Wang, "Sliding mode controller based on feedback linearization for damping of sub-synchronous control interaction in DFIG-based wind power plants," *International Journal of Electrical Power & Energy Systems*, vol. 107, pp. 239-250, 2019/05/01/ 2019.
- [13] P. Li, L. Xiong, M. Ma, S. Huang, Z. Zhu, and Z. Wang, "Energy-shaping L2-gain controller for PMSG wind turbine to mitigate subsynchronous interaction," *International Journal of Electrical Power & Energy Systems*, vol. 135, p. 107571, 2022/02/01/ 2022.
- [14] D. Wu, F. Tang, T. Dragicevic, J. C. Vasquez, and J. M. Guerrero, "Autonomous Active Power Control for Islanded AC Microgrids With Photovoltaic Generation and Energy Storage System," *IEEE Transactions on Energy Conversion*, vol. 29, no. 4, pp. 882-892, 2014.
- [15] T.-T. Nguyen, H.-J. Yoo, and H.-M. Kim, "Application of model predictive control to BESS for microgrid control," *Energies*, vol. 8, no. 8, pp. 8798-8813, 2015.
- [16] Y. Shan, J. Hu, Z. Li, and J. M. Guerrero, "A Model Predictive Control for Renewable Energy Based AC Microgrids Without Any PID Regulators," *IEEE Transactions on Power Electronics*, vol. 33, no. 11, pp. 9122-9126, 2018.
- [17] M. Cucuzzella, G. P. Incremona, and A. Ferrara, "Decentralized Sliding Mode Control of Islanded AC Microgrids With Arbitrary Topology," *IEEE Transactions on Industrial Electronics*, vol. 64, no. 8, pp. 6706-6713, 2017.
- [18] G. P. Incremona, M. Cucuzzella, and A. Ferrara, "Adaptive suboptimal second-order sliding mode control for microgrids," *International Journal of Control*, vol. 89, no. 9, pp. 1849-1867, 2016/09/01 2016.
- [19] M. Cucuzzella, G. P. Incremona, and A. Ferrara, "Design of robust higher order sliding mode control for microgrids," *IEEE Journal on Emerging Selected Topics in Circuits Systems*, vol. 5, no. 3, pp. 393-401, 2015.
- [20] A. Ferrara, G. P. Incremona, and M. Cucuzzella, *Advanced and optimization based sliding mode control: Theory and applications*. SIAM, 2019.
- [21] M. N. Undeland, W. P. Robbins, and N. Mohan, "Power electronics," in *Converters, Applications, and Design*: John Wiley & Sons, 1995.
- [22] B. Yang *et al.*, "Perturbation observer based fractional-order sliding-mode controller for MPPT of grid-connected PV inverters: Design and real-time implementation," *Control Engineering Practice*, vol. 79, pp. 105-125, 2018.
- [23] B. Yang *et al.*, "Applications of supercapacitor energy storage systems in microgrid with distributed generators via passive fractional-order sliding-mode control," *Energy*, vol. 187, p. 115905, 2019.

- [24] R. Errouissi, A. Al-Durra, and S. M. Mueen, "A Robust Continuous-Time MPC of a DC–DC Boost Converter Interfaced With a Grid-Connected Photovoltaic System," *IEEE Journal of Photovoltaics*, vol. 6, no. 6, pp. 1619-1629, 2016.
- [25] C. Yeong Jia and E. K. K. Sng, "A novel communication strategy for decentralized control of paralleled multi-inverter systems," *IEEE Transactions on Power Electronics*, vol. 21, no. 1, pp. 148-156, 2006.
- [26] A. Rosini, A. Bonfiglio, and R. Procopio, "On The Use of Frequency in the Primary Control of fully Inverter Based Islanded Microgrids," *International Journal of Electrical Power and Energy Systems*, 2022.
- [27] G. Bartolini, A. Ferrara, and E. Usai, "Chattering avoidance by second-order sliding mode control," *IEEE Transactions on automatic control*, vol. 43, no. 2, pp. 241-246, 1998.
- [28] J. Rocabert, A. Luna, F. Blaabjerg, and P. Rodríguez, "Control of Power Converters in AC Microgrids," *IEEE Transactions on Power Electronics*, vol. 27, no. 11, pp. 4734-4749, 2012.
- [29] A. Ferrara, G. P. Incremona, and M. Cucuzzella, "Chapter 2: Introduction to Higher Order Sliding Mode Control," in *Advanced and Optimization Based Sliding Mode Control: Theory and Applications*(Advances in Design and Control: Society for Industrial and Applied Mathematics, 2019, pp. 33-52.
- [30] U. Boke, "A simple model of photovoltaic module electric characteristics," in *2007 European Conference on Power Electronics and Applications*, 2007, pp. 1-8: IEEE.
- [31] R. A. DeCarlo, S. H. Zak, and G. P. Matthews, "Variable structure control of nonlinear multivariable systems: a tutorial," *Proceedings of the IEEE*, vol. 76, no. 3, pp. 212-232, 1988.
- [32] A. Palmieri, A. Rosini, R. Procopio, and A. Bonfiglio, "An MPC-Sliding Mode Cascaded Control Architecture for PV Grid-Feeding Inverters," *Energies*, vol. 13, no. 9, p. 2326, 2020.
- [33] A. Bonfiglio *et al.*, "Modeling and Experimental Validation of an Islanded No-Inertia Microgrid Site," *IEEE Transactions on Sustainable Energy*, vol. 9, no. 4, pp. 1812-1821, 2018.
- [34] D. Raverkar, U. Chauhan, V. Singh, and A. Rani, "An Improved Fractional Voltage Based MPPT Technique for PV Generation System," in *2020 International Conference on Advances in Computing, Communication & Materials (ICACCM)*, 2020, pp. 267-271.
- [35] ENTSO-E, "Network Code for Requirements for Grid Connection Applicable to all Generators (NC RfG), March 2013," ed.
- [36] J.-J. E. Slotine and W. Li, *Applied nonlinear control* (no. 1). Prentice hall Englewood Cliffs, NJ, 1991.